RESEARCH ARTICLE

Preparation of Ni-Mn ferrites magnetic nanoparticles through the ethanol solution combustion-calcination process for the adsorption of methyl blue

Zhongjun Pan[1], Zhou Wang[2], Zhixiang Lv[1]*

1 The People's Hospital of Danyang, Affiliated Danyang Hospital of Nantong University, Zhenjiang, P.R. China, **2** College of Vanadium and Titanium, Panzhihua University, Panzhihua, P.R. China

* dylvzhixiang@163.com

Abstract

Ni-Mn ferrites magnetic nanoparticles (MNPs) were successfully prepared through the ethanol solution combustion-calcination process, and characterized by SEM, TEM, XRD, VSM, BET, and FTIR techniques. For smaller particle size and suitable magnetic property, the optimum element ratio of the material was $Ni_{0.9}Mn_{0.1}Fe_2O_4$, and the optimal preparation conditions were appropriate ethanol dosage to attain Fe^{3+} concentrations of approximately 0.85 M, calcination temperature of 400 °C, and calcination time of 2 h, their specific surface area was 136.5 m^2/g, and their average particle size and saturation magnetization were 35 nm and 21.66 emu/g, respectively. The adsorption process of methyl blue (MB) onto $Ni_{0.9}Mn_{0.1}Fe_2O_4$ MNPs conformed to the pseudo-second-order adsorption kinetic model in the initial concentrations of 100–250 mg/L. In comparison with Langmuir and Freundlich adsorption isotherm models, the Temkin model (R^2 = 0.9865) was observed to better demonstrate the state of MB onto $Ni_{0.9}Mn_{0.1}Fe_2O_4$ MNPs, revealing that the adsorption mechanism of MB onto $Ni_{0.9}Mn_{0.1}Fe_2O_4$ MNPs was the multi-molecular chemical process. The adsorption capacity of $Ni_{0.9}Mn_{0.1}Fe_2O_4$ MNPs for MB still maintained about 90% of the initial adsorbance after 6 times cyclic utilization of the nanoparticles by recalcination method, suggesting that $Ni_{0.9}Mn_{0.1}Fe_2O_4$ MNPs had excellent regeneration performance. In general, these results coupled with its environmental friendliness attributed the potential candidates for effluent remediation.

OPEN ACCESS

Citation: Pan Z, Wang Z, Lv Z (2025) Preparation of Ni-Mn ferrites magnetic nanoparticles through the ethanol solution combustion-calcination process for the adsorption of methyl blue. PLoS One 20(5): e0321741. https://doi.org/10.1371/journal.pone.0321741

Editor: Bing Xu, Brandeis University, UNITED STATES OF AMERICA

Received: December 20, 2024

Accepted: March 11, 2025

Published: May 9, 2025

Data availability statement: All relevant data are within the paper and its Supporting information files.

Funding: The author(s) received no specific funding for this work.

1. Introduction

The issue of pollution is increasingly becoming more severe, and has aroused human's great attention, including water and atmospheric pollution, soil degradation, noise disturbance, and other forms of pollution [1–4]. Among these concerns, water

Competing interests: The authors have declared that no competing interests exist.

pollution has gained increasing prominence due to the extreme scarcity of freshwater resources [5,6]. Especially, dye-containing effluent attaches great importance as it has posed a grave threat on water environment and human health, even human life, owing to its high toxicity, chemical stability, and slow degradation rate [7,8]. However, according to statistics, about 80% of the dye effluent is discharged into the environment without treatment [9].

The treatment of these effluents has been listed as the focus of environmental protection. An effective measure is badly necessitated. A variety of techniques have been developed to eliminate dye-based pollutants from water solutions, including physical method [10], chemical process [11–13], biological process [14,15], and so on. Among them, as the physical method, adsorption has garnered significant attention due to its cost-effectiveness and superior efficiency [16,17]. Additionally, the chemical decomposition or transformation of pollutants is not presented in the adsorption process, thus avoiding the generation of new contaminants. What's more, the adsorption process occurs the surface of adsorbents, including outside surface and internal surface, thus the adsorbents play a significant pivotal role [18].

At present, the commonly used adsorbents include activated carbon, polymer resin and mineral adsorbents, etc., but they all have certain limitations, such as difficulty in regeneration, operational complexity and, most importantly, the limitation in adsorption capacity [19,20]. Compared with conventional adsorbents, nanoparticles have attracted much more attention owing to their large specific surface area and large adsorption capacity [21]. However, practical applications can be inconvenienced by the difficulty of collecting nanoparticles from their dispersing media. In this context, magnetic nanoparticles, which can be easily recycled with an external magnetic field [22], thus facilitating the application and cost management of magnetic nanoparticles while minimizing the number of material syntheses [23–25], are one of the desirable candidate adsorbents for effluent treatment. Particularly, spinel ferrites (MFe_2O_4) nanoparticles, providing excellent magnetic susceptibility, functionalization potential, low cost as well as unique advantages in regenerating and recycling, are among the most promising of these compounds [26].

There are many preparation methods for magnetic ferrite-based nanoparticles, such as precipitation, sol-gel, hydrothermal, high-energy ball milling [27,28], etc. As a new preparation method, the ethanol solution combustion-calcination process has the advantages of simple work-up procedure, shorter reaction time and preparation cycle, low cost, environmental friendliness, low requirements on the equipment, easy realization of industrialized production, and so on.

For the purpose of developing a nanomaterial with high adsorption capacity and satisfactory recycling performance, $Ni_{0.9}Mn_{0.1}Fe_2O_4$ MNPs prepared through the ethanol solution combustion-calcination process were selected and employed to remove dyes in this work, and with methyl blue (MB) as adsorbate model, the adsorption performance of the azo dyes on $Ni_xMn_{(1-x)}Fe_2O_4$ MNPs from water solution was explored [29,30].

2. Experiments

2.1. *Preparation and characterization of Ni-Mn ferrites MNPs*

$Ni_xMn_{(1-x)}Fe_2O_4$ MNPs were prepared through the ethanol solution combustion-calcination process using absolute ethanol as solvent and fuel. $Fe(NO_3)_3{\cdot}9H_2O$, $Ni(NO_3)_2{\cdot}6H_2O$, and $Mn(NO_3)_2{\cdot}4H_2O$ were precisely weighed according to the stoichiometric ratio, and dissolved in a beaker with anhydrous ethanol as a solvent to achieve Fe^{3+} concentrations of about 0.85 M, 0.57 M, 0.43 M, 0.34 M, and 0.17 M, respectively. When all the nitrates were completely dissolved to form homogeneous solutions, the solutions were transferred into crucibles and ignited. After the flames were extinguished, the crucibles together with intermediates were calcined at various temperatures (400 °C, 500 °C, 600 °C, and 700 °C) for 2 h. Finally, the calcined products were placed in a mortar and ground to form powders.

The phase identification of Ni-Mn ferrites MNPs was measured by XRD and FTIR, the morphology was investigated with SEM and TEM, the chemical composition was detected by EDS, the magnetic measurement was examined by VSM, and the specific surface area was measured by BET method.

2.2. *Adsorption of MB onto $Ni_{0.9}Mn_{0.1}Fe_2O_4$ MNPs*

$Ni_{0.9}Mn_{0.1}Fe_2O_4$ MNPs were selected to remove MB. At ambient temperature, adsorption kinetics experiments were performed by keeping 5 mg of $Ni_{0.9}Mn_{0.1}Fe_2O_4$ MNPs in a series of centrifuge tubes containing 2 mL MB solution with initial concentrations (100, 150, 200, and 250 mg/L). The adsorbents were subsequently separated at regular intervals (10–180 min), and the adsorption capacities of $Ni_{0.9}Mn_{0.1}Fe_2O_4$ MNPs were determined based on the change of MB concentration.

The adsorption isotherm of MB onto the nanoparticles was investigated by the similar method, 10 different initial concentrations of MB solution ranging from 400 mg/mL to 4000 mg/mL were adsorbed for 24 h. Subsequently, the supernatants of different initial concentrations were measured.

Additionally, to explore the influence of pH on adsorbance of MB onto $Ni_{0.9}Mn_{0.1}Fe_2O_4$ MNPs, the pH values of 1, 3, 5, 7, 9, 11, and 13 were adjusted by 1 M dilute HCl or dilute NaOH solutions of, and the adsorption capacities under various pH values were obtained. As to the cycle capacity of $Ni_{0.9}Mn_{0.1}Fe_2O_4$ MNPs [31], 75 mg $Ni_{0.9}Mn_{0.1}Fe_2O_4$ MNPs were dispersed into 30 mL MB of 500 mg/L in Erlenmeyer flask for 3 h. Upon completion of the adsorption, $Ni_{0.9}Mn_{0.1}Fe_2O_4$ MNPs were centrifuged and recalcined at 400 °C for 2 h to regenerate the nanoparticles. The experiment described above was replicated after grinding and the adsorption process of MB onto $Ni_{0.9}Mn_{0.1}Fe_2O_4$ MNPs was verified by infrared spectroscopy.

The absorbances of MB solutions were detected using a UV-Vis spectrophotometer at 600 nm, and the corresponding concentrations were obtained according to the relationship of the absorbance and MB concentration; while, the adsorbance of MB loaded onto $Ni_{0.9}Mn_{0.1}Fe_2O_4$ MNPs was calculated Using Eq. (1) [32].

$$q_e = \frac{V(C_0 - C_e)}{m} \tag{1}$$

Wherein, q_e represented the equilibrium adsorbance of MB onto $Ni_{0.9}Mn_{0.1}Fe_2O_4$ MNPs; m was the mass of $Ni_{0.9}Mn_{0.1}Fe_2O_4$ MNPs; V indicated the volume of MB solution; C_0 and C_e were the initial and equilibrium concentrations [18].

3. Results and discussion

3.1. *Characteristics of $Ni_{0.9}Mn_{0.1}Fe_2O_4$ MNPs*

Fig 1 showed the characteristics of $Ni_{0.9}Mn_{0.1}Fe_2O_4$ MNPs calcined at 400 °C with 20 mL ethanol to achieve a Fe^{3+} concentration of 0.85 M. The SEM morphology (Fig 1A/S1 Fig) displayed that their average particle size was about 35 nm, and the distribution of the particle sizes was uniform. The TEM image (Fig 1B/S2 Fig) suggested that the average particle size of $Ni_{0.9}Mn_{0.1}Fe_2O_4$ MNPs was also approximately 35 nm, which was consistent with the result from SEM morphology. The EDS

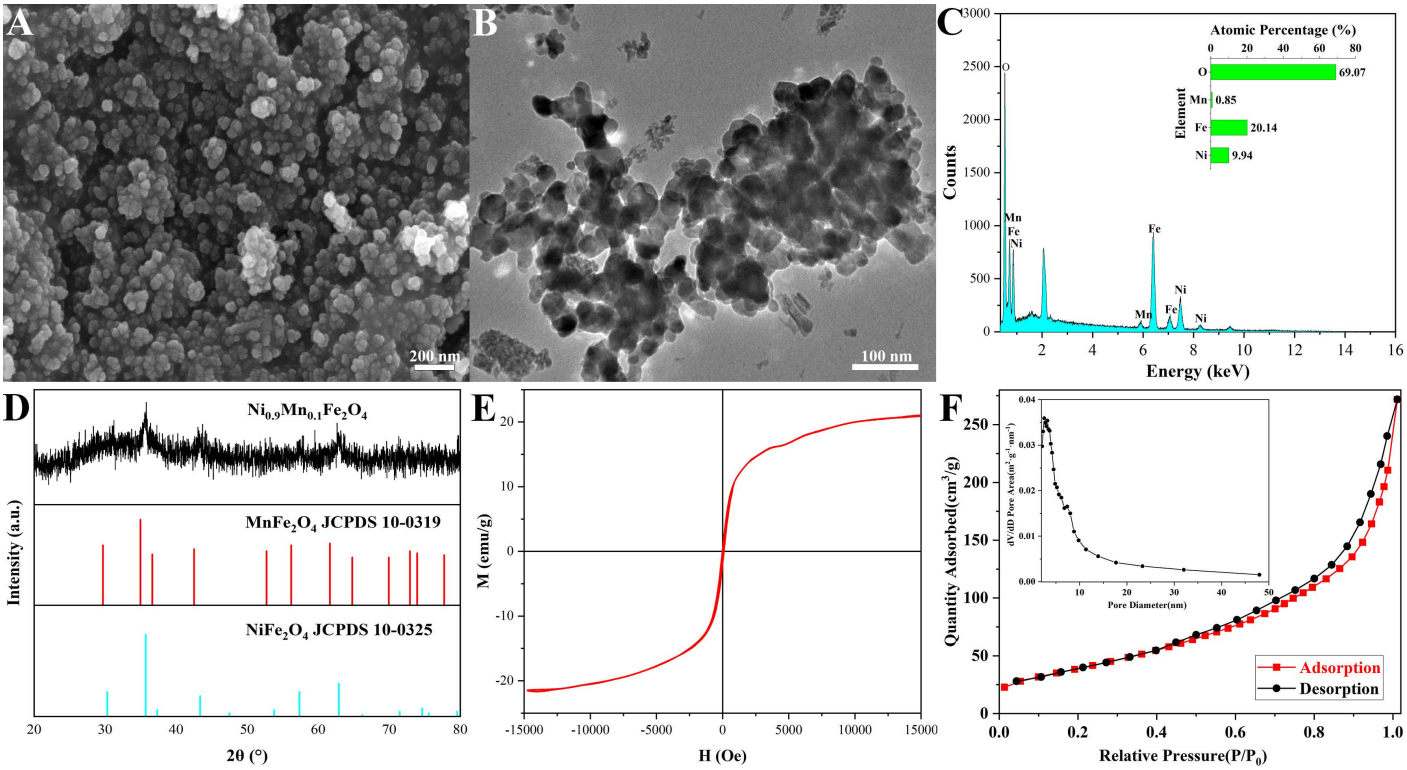

Fig 1. SEM morphology (A), TEM image (B), EDS spectrum (C), XRD pattern (D), the hysteresis loops (E), and N_2 sorption isotherm (F) of $Ni_{0.9}Mn_{0.1}Fe_2O_4$ MNPs calcined at 400 °C with 20 mL ethanol and Fe^{3+} concentrations of 0.85 M.

https://doi.org/10.1371/journal.pone.0321741.g001

spectrum was displayed in Fig 1C, the atomic percentages of Ni, Mn, Fe and O in $Ni_{0.9}Mn_{0.1}Fe_2O_4$ MNPs were basically consistent with the designed composition, which revealed the successful preparation of magnetic $Ni_{0.9}Mn_{0.1}Fe_2O_4$ nanoparticles. The crystal structures of the $Ni_{0.9}Mn_{0.1}Fe_2O_4$ nanoparticles were investigated by XRD. Fig 1D illustrated that the based diffraction peaks of $Ni_{0.9}Mn_{0.1}Fe_2O_4$ MNPs could be indexed to the standard $NiFe_2O_4$ PDF card (JCPDS No. 10–0325) and $MnFe_2O_4$ PDF card (JCPDS No. 10–0319). Fig 1E displayed the hysteresis loops of $Ni_{0.9}Mn_{0.1}Fe_2O_4$ MNPs with typical soft magnetic characteristic, their saturation magnetization (Ms) was about 21.66 emu/g, which demonstrated the superparamagnetism of the material [25,33]. All these results indicated that $Ni_{0.9}Mn_{0.1}Fe_2O_4$ MNPs were successfully prepared. Fig 1F showed the N_2 sorption isotherm of $Ni_{0.9}Mn_{0.1}Fe_2O_4$ MNPs, the adsorption-desorption isotherm curve belonged to the type of IV, and an obvious hysteresis ring appeared, the specific surface area of $Ni_{0.9}Mn_{0.1}Fe_2O_4$ MNPs was 136.5 m^2/g, and their average pore size distributed from 2 nm to 10 nm, the numerous inner bores contributed to large specific surface area, and the large specific surface area was the important factor for the large adsorption capacity of $Ni_{0.9}Mn_{0.1}Fe_2O_4$ MNPs.

3.2. *Optimization of preparation process for NixMn(1-x)Fe2O4 MNPs*

3.2.1. *Influence of element proportion.* It could be seen from Fig 2A that when x = 0.1–0.5, there were no obvious characteristic peaks in the spectra, which might ascribe to the fact that the nanoparticles failed to form stable crystallization at this time, and was disregarded. When x = 0.6–0.9, there were obvious characteristic peaks. When x = 0.9, the characteristic peak was the widest, suggesting that the crystallinity was the lowest, and their average particle size of $Ni_xMn_{(1-x)}Fe_2O_4$ MNPs was the smallest. Fig 2B showed the hysteresis loops obtained by measuring the performance of $Ni_xMn_{(1-x)}Fe_2O_4$ (x = 0.1–0.9) MNPs by vibrating sample magnetometer. The saturation magnetization of magnetic

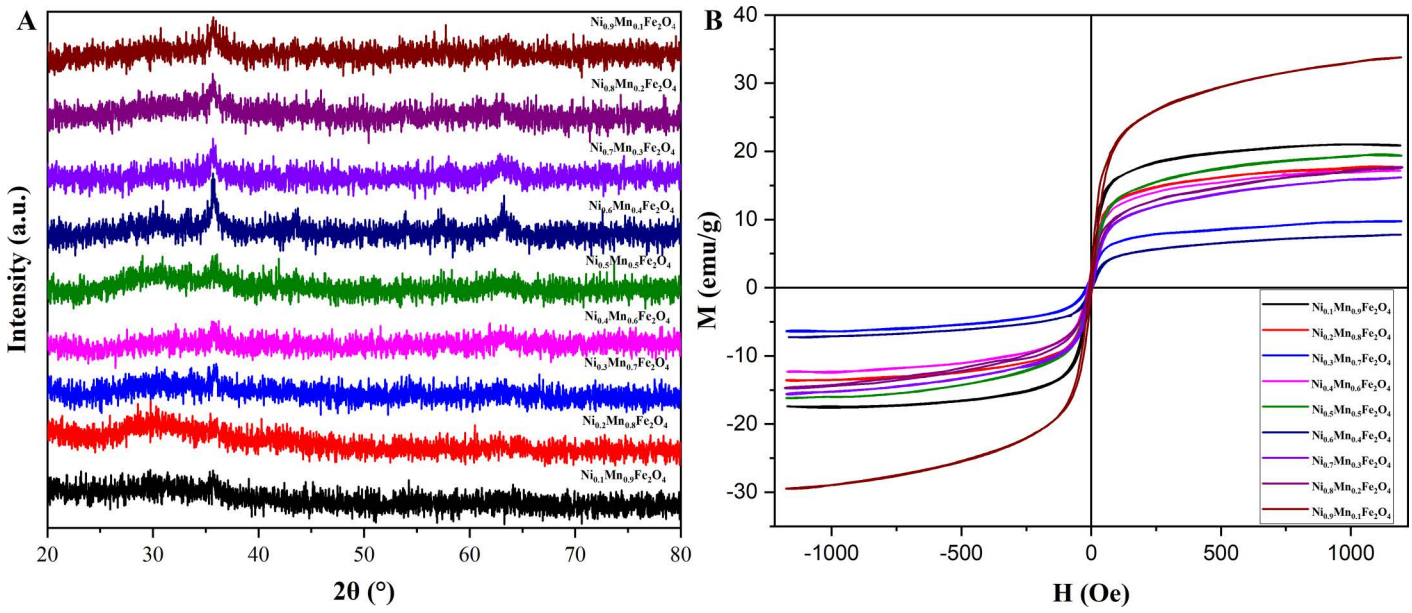

Fig 2. XRD pattern (A) and hysteresis loops (B) of $Ni_xMn_{(1-x)}Fe_2O_4$ (x = 0.1–0.9) MNPs with different element ratios.

https://doi.org/10.1371/journal.pone.0321741.g002

$Ni_{0.9}Mn_{0.1}Fe_2O_4$ nanoparticles was the highest of 33.80 emu/g, which provided a guarantee for the separation and recovery of $Ni_{0.9}Mn_{0.1}Fe_2O_4$ nanoparticles.

3.2.2. ***Effects of calcination temperature and ethanol dosage.*** Fig 3A revealed the XRD patterns of $Ni_{0.9}Mn_{0.1}Fe_2O_4$ MNPs prepared at 400 °C for 2 h with various ethanol volumes for Fe^{3+} concentrations of about 0.85 M, 0.57 M, 0.43 M, 0.34 M, and 0.17 M, respectively. The change of the ethanol dosage would affect the combustion time and the dispersion degree of the preparation process, thus affect the grain size. As was well-known, the long combustion time could increase the degree of crystallinity, and the large dispersion degree of mental ions could reduce the degree of crystallinity. At low doses of ethanol solvent, i.e., large Fe^{3+} concentrations, the combustion time of the ingredient solution was short, and the dispersion degree of mental ions was low, but the combustion time played a mainly larger effect; therefore, with Fe^{3+} concentrations changing from 0.85 M to 0.34 M, the degree of crystallinity increased, and the diffraction peak became narrower and higher. However, with Fe^{3+} concentrations reaching 0.17 M, the dispersion degree of the mental ions began to play the larger effect, resulting in the decrease of the crystallinity degree, therefore, the diffraction peak became shorter and wider, and the average particle size increased. Fig 3B showed the hysteresis loops of $Ni_{0.9}Mn_{0.1}Fe_2O_4$ MNPs with different concentrations of ingredient solutions. Obviously, the nanoparticles retained excellent magnetic properties even at low doses (i.e., Fe^{3+} concentration of 0.85 M). With the decrease of Fe^{3+} concentration, the degree of crystallinity increased, Ms of $Ni_{0.9}Mn_{0.1}Fe_2O_4$ MNPs increased. When Fe^{3+} concentration reached 0.17 M, the degree of crystallinity decreased, Ms of $Ni_{0.9}Mn_{0.1}Fe_2O_4$ MNPs also decreased [34]. Based on the above analysis, to obtain the nanoparticles with larger adsorption performance, the Fe^{3+} concentration of the raw material solution for the preparation of $Ni_{0.9}Mn_{0.1}Fe_2O_4$ MNPs was selected as 0.85 M.

Fig 3C displayed the XRD patterns of $Ni_{0.9}Mn_{0.1}Fe_2O_4$ MNPs calcined at 400 °C, 500 °C, 600 °C, and 700 °C for 2 h with Fe^{3+} concentration of 0.85 M. The diagram indicated that the characteristic peaks were more prominent with the rise of calcination temperature. When the calcination temperature was 400 °C, the characteristic peaks were the widest and the lowest. Too high temperature would cause the material to agglomerate and increase the particle size, resulting in the decreases of the specific surface area owing to the decrease of inner bore, and finally a descent of the adsorbance. Moreover, with the increase of calcination temperature, the pores inside the nanoparticles would collapse, which would

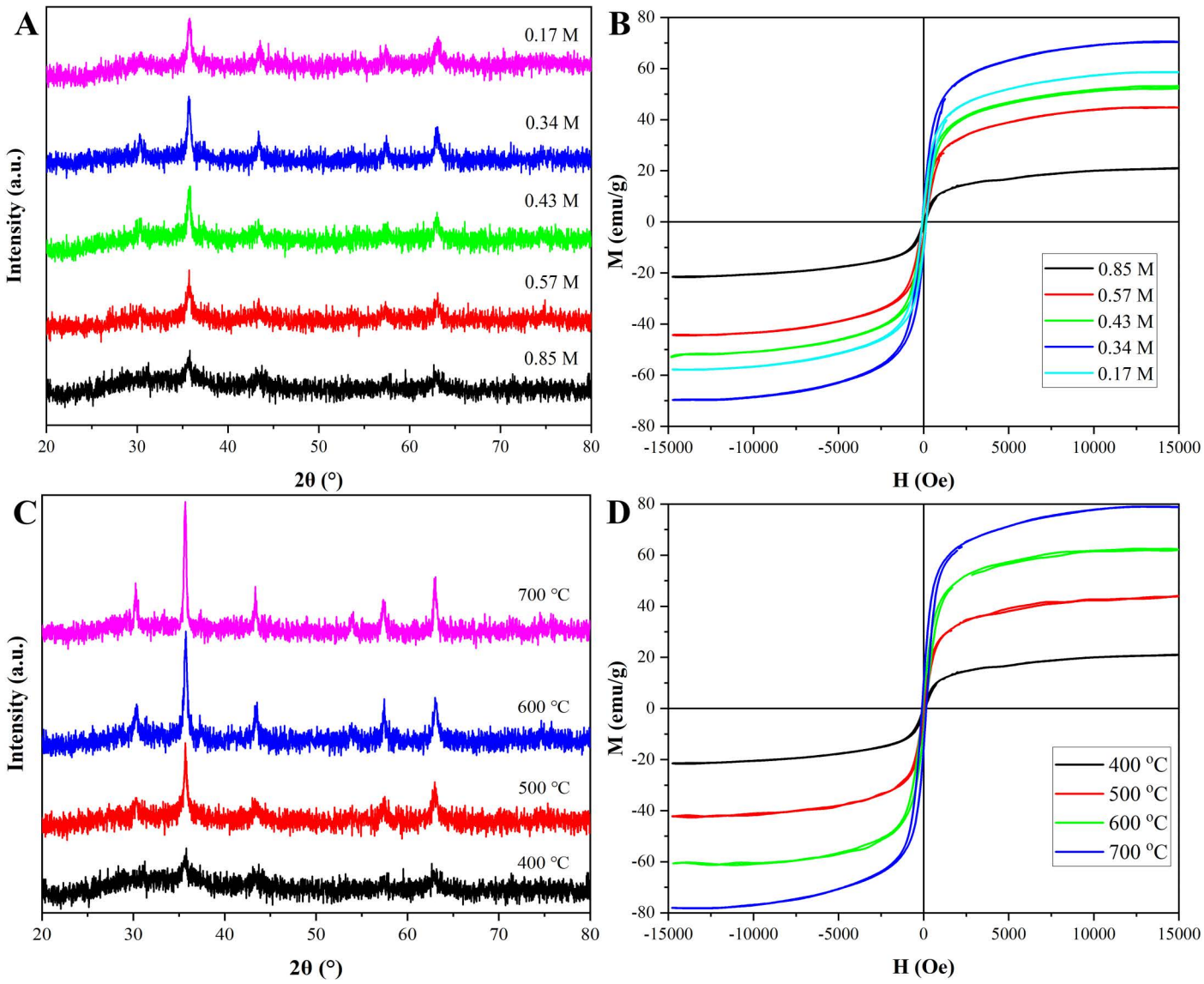

Fig 3. XRD patterns (A, B) and hysteresis loops (C, D) of $Ni_{0.9}Mn_{0.1}Fe_2O_4$ MNPs prepared with different Fe^{3+} concentrations and at various temperatures.

https://doi.org/10.1371/journal.pone.0321741.g003

also lead to poor adsorption performance. Fig 3D displayed the hysteresis loops of $Ni_{0.9}Mn_{0.1}Fe_2O_4$ MNPs calcined at different temperatures, and the saturation magnetization strength of the nanoparticles similarly increased with the rise of calcination temperature. Although higher temperatures leaded to better magnetic properties, they also leaded to too large nanoparticle size, which made adsorption capacity decrease. Considering comprehensively, the sample calcined at 400 °C should be selected for the next experiments.

3.3. *Adsorption of MB onto $Ni_{0.9}Mn_{0.1}Fe_2O_4$ MNPs*

3.3.1. *Adsorption kinetics.* To explore the adsorption mechanism, different models were employed to fit the adsorption data, and the adsorbance of MB onto $Ni_{0.9}Mn_{0.1}Fe_2O_4$ MNPs with time was investigated by fitting the curve and

kinetics parameters. For this assessment, the pseudo-first-order, pseudo-second-order and intraparticle diffusion models as expressed in Eq. (2) [35], Eq. (3) [18] and Eq. (4) [36] were applied.

$$q_t = q_e(1 - e^{k_1 t}) \tag{2}$$

$$q_t = \frac{q_e^2 k_2 t}{1 + q_e k_2 t} \tag{3}$$

$$q_t = x_i + k_i t^{1/2} \tag{4}$$

Wherein, q_e and q_t were the adsorbances of MB onto $Ni_{0.9}Mn_{0.1}Fe_2O_4$ MNPs at equilibrium time and a given time; k_1, k_2 and k_i were the rate constants for three models; x_i was associated to the thickness of boundary layer.

The experimental curves for the adsorption of MB onto $Ni_{0.9}Mn_{0.1}Fe_2O_4$ MNPs with various initial MB concentrations at room temperature with time were revealed in Fig 4. The adsorbances of MB onto $Ni_{0.9}Mn_{0.1}Fe_2O_4$ MNPs rose with the increase of the initial MB concentration. Under the same concentration, the adsorption rate was fast followed by slow until

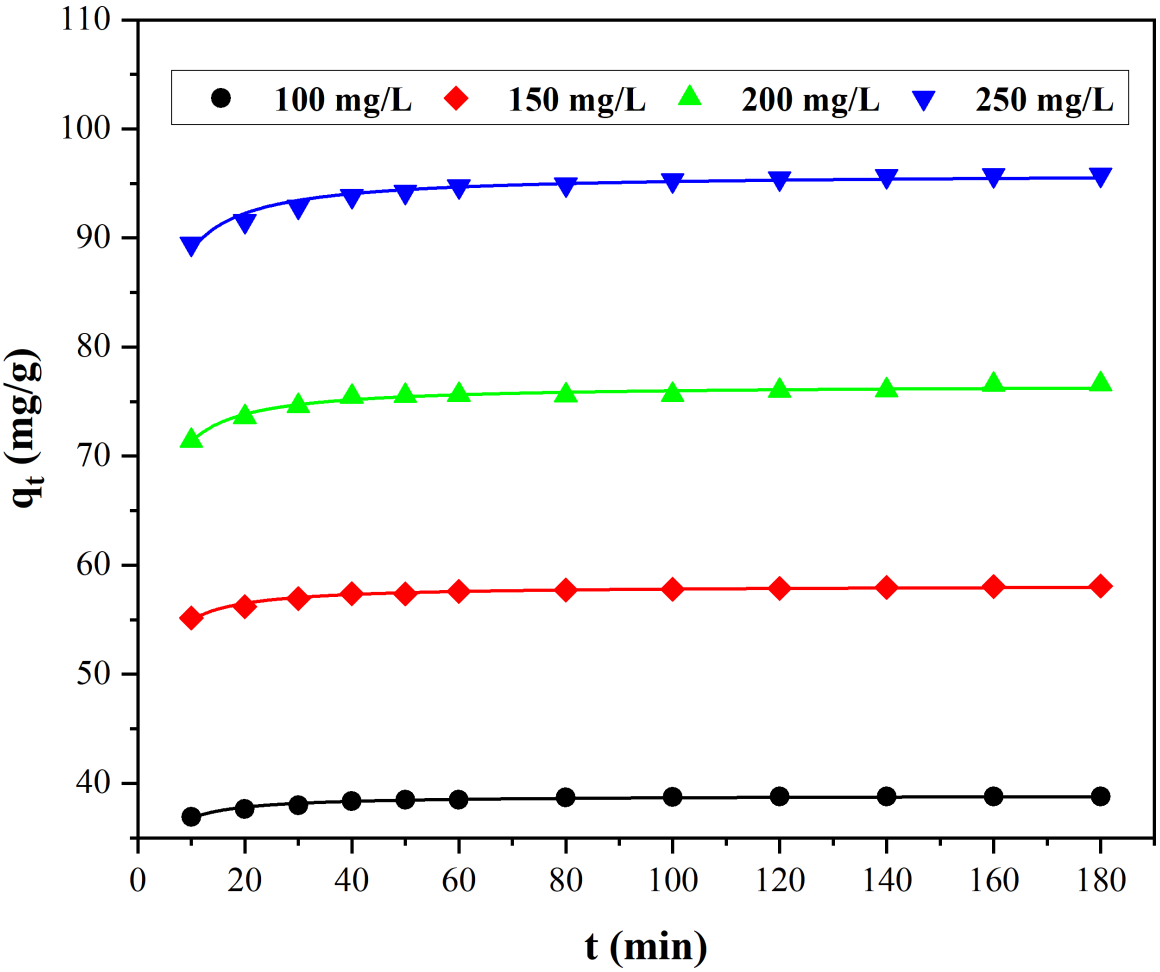

Fig 4. Adsorption process of MB onto $Ni_{0.9}Mn_{0.1}Fe_2O_4$ MNPs for various initial MB concentrations at room temperature.

https://doi.org/10.1371/journal.pone.0321741.g004

the equilibrium was reached. The fitted curves with three kinetic models for MB onto $Ni_{0.9}Mn_{0.1}Fe_2O_4$ MNPs were presented in Fig 5, and all the fitted kinetic parameters were listed in Table 1. The pseudo-second-order kinetics model showed the best fitting based on the variances (R^2) for three models, and their variances were larger than 0.96, and the line relationships of the pseudo second-order adsorption kinetic model for the adsorption of MB onto $Ni_{0.9}Mn_{0.1}Fe_2O_4$ MNPs with various MB initial concentrations were displayed in Fig 6, which revealed better line correlations, all the results suggested that the adsorption of MB onto $Ni_{0.9}Mn_{0.1}Fe_2O_4$ MNPs might be a chemical adsorption involving electron sharing or electron transfer.

3.3.2. ***Adsorption isotherms.*** The adsorption isotherm could provide the interaction relationship of MB molecules and the state of MB on the surfaces of $Ni_{0.9}Mn_{0.1}Fe_2O_4$ MNPs. Therefore, Langmuir, Freundlich, and Temkin adsorption isotherm models were employed to simulate the adsorption equilibrium curves.

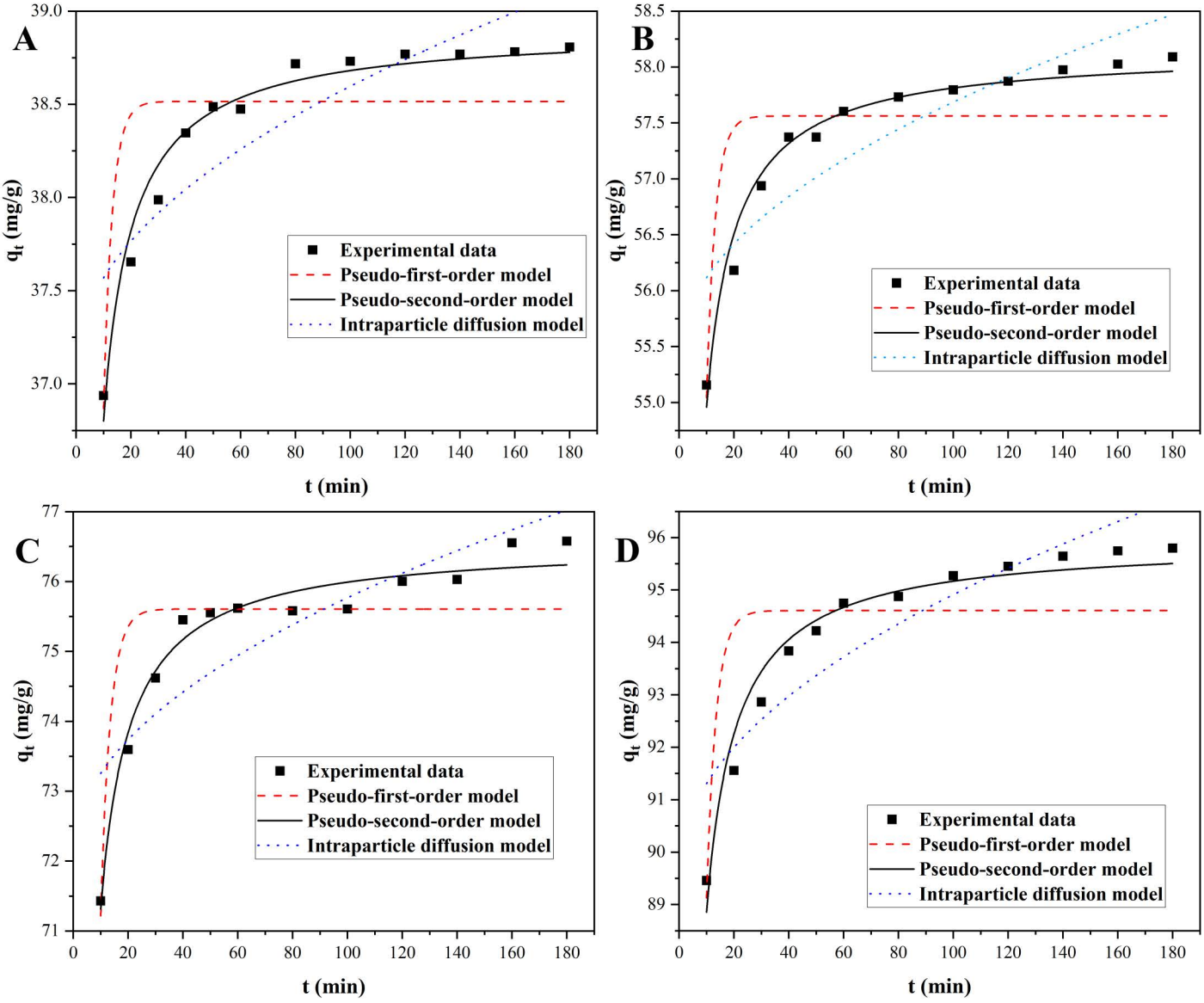

Fig 5. The fitting curves for three kinetics models with initial MB concentrations of 100 mg/L (A), 150 mg/L (B), 200 mg/L (C), and 250 mg/L (D).

https://doi.org/10.1371/journal.pone.0321741.g005

Table 1. The simulative adsorption kinetics parameters for MB onto $Ni_{0.9}Mn_{0.1}Fe_2O_4$ MNPs at room temperature.

Adsorption kinetics model	parameter	initial concentrations of MB (mg/L)			
		100	150	200	250
pseudo-first-order kinetics	R^2	0.6432	0.6523	0.7252	0.6097
	K_1	0.3151	0.3129	0.2846	0.2848
	Adj. R^2	0.6076	0.6176	0.6977	0.5707
pseudo-second-order kinetics	R^2	0.9776	0.9760	0.9710	0.9625
	K_2	0.0450	0.0296	0.0178	0.0131
	Adj. R^2	0.9695	0.9737	0.9682	0.9587
internal diffusion	R^2	0.7521	0.7638	0.7212	0.8120
	K_i	0.1502	0.2295	0.3674	0.5272
	Adj. R^2	0.7274	0.7402	0.6933	0.7932

https://doi.org/10.1371/journal.pone.0321741.t001

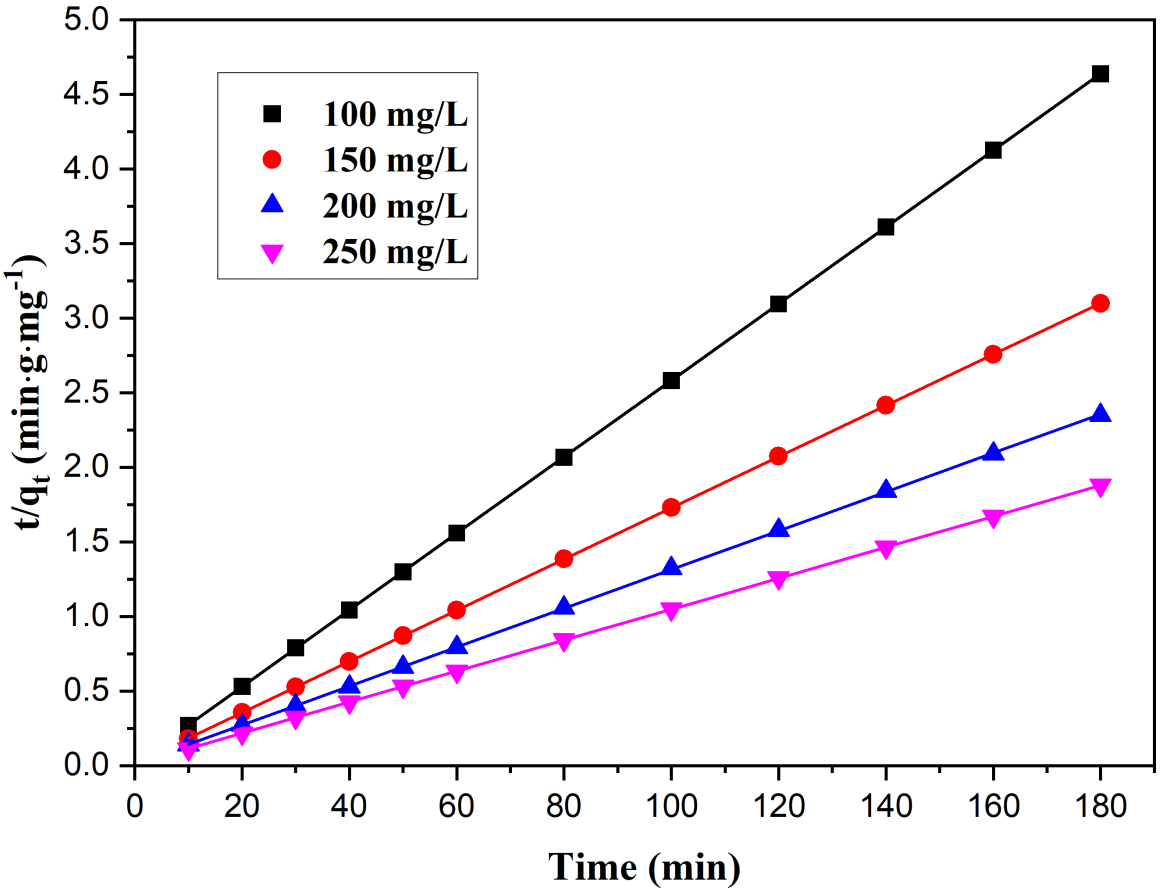

Fig 6. Plots of t/q_t versus t for adsorption of MB onto magnetic $Ni_{0.9}Mn_{0.1}Fe_2O_4$ MNPs with the various initial concentrations at room temperature.

https://doi.org/10.1371/journal.pone.0321741.g006

Langmuir model could be described by the Eq. (5) [37].

$$q_e = \frac{q_{\max} K_L C_e}{1 + K_L C_e} \tag{5}$$

wherein q_e and q_{max} were the equilibrium and the maximum adsorbances of MB onto $Ni_{0.9}Mn_{0.1}Fe_2O_4$ MNPs, C_e was the equilibrium concentration of MB, and K_L was the rate of adsorption.

Freundlich model assumed that the adsorption of adsorbate onto adsorbent was bistratal, and its equation was described by Eq. (6) [30].

$$q_e = K_F C_e^{\frac{1}{n}} \tag{6}$$

Whereas K_F was a constant for Freundlich model. 1/n was a dimensionless factor that reflected the adsorption intensity or surface heterogeneity.

Temkin model assumed that the adsorption of adsorbate onto adsorbent was tanglesome, and its expression was shown as Eq. (7) [38].

$$q_e = B \ln(A_T C_e) \tag{7}$$

Wherein, B and A_T were the constant for Temkin and the equilibrium binding constant, respectively.

Nonlinear regression methods were utilized to fit the equilibrium data and evaluate the parameters associated with these models, and the fitting curves were displayed in Fig 7, and the simulative parameters were demonstrated in Table 2. Comparing their R^2, Temkin model acquired the best fitting, and its R^2 value reached 0.9865, which indicated that Temkin model was most suitable for explain the adsorption state of MB onto $Ni_{0.9}Mn_{0.1}Fe_2O_4$ MNPs. According to the theory of Temkin isothermal model, the adsorption of MB onto $Ni_{0.9}Mn_{0.1}Fe_2O_4$ MNPs should belong to multi-molecular layer chemical adsorption mechanism [39].

3.3.3. ***Effect of pH on adsorbance and regeneration study.*** The pH of MB solution had significant impact on the adsorption, because pH not only affected the surface charge of $Ni_{0.9}Mn_{0.1}Fe_2O_4$ MNPs, but also affected the property of the dye itself [40]. To reveal the influence of pH on the adsorbance of MB onto $Ni_{0.9}Mn_{0.1}Fe_2O_4$ MNPs, the experiments were carried out with various pH of MB solution and the initial MB concentration of 200 mg/L, and the effect of pH on the adsorption was displayed in Fig 8A. When the pH exceeded 5, the adsorption capacity of MB onto $Ni_{0.9}Mn_{0.1}Fe_2O_4$ MNPs remained a large value. However, once the pH was less than 5, the adsorption capacity decreased sharply. The reason for this phenomenon was that the surface of $Ni_{0.9}Mn_{0.1}Fe_2O_4$ MNPs was positively charged owing to MB isoelectric point of about 5. When the pH was less than 5, the surface of MB was positively charged, and there was an electrostatic repulsion between MB and $Ni_{0.9}Mn_{0.1}Fe_2O_4$ MNPs, which gradually decreased with the increase of pH value. As the pH was greater than 5, MB was negatively charged, the dissimilar electrostatics resulted in combination of MB and $Ni_{0.9}Mn_{0.1}Fe_2O_4$ MNPs, and the adsorption capacity reached the maximum, and did not change, suggesting that the saturated adsorption state had been reached at this time. In short, the nanoparticles could maintain a large adsorption capacity for MB in a large pH range from 5 to 13.

The regeneration of $Ni_{0.9}Mn_{0.1}Fe_2O_4$ MNPs was shown in Fig 8B. With the increase in reuse frequency of $Ni_{0.9}Mn_{0.1}Fe_2O_4$ MNPs, the adsorbance of MB onto $Ni_{0.9}Mn_{0.1}Fe_2O_4$ MNPs gradually reduced. This might be attributed to the fact that the repeated calcination process increased the sintering degree of $Ni_{0.9}Mn_{0.1}Fe_2O_4$ MNPs and the proportion of pore collapse, resulting in a decrease of their specific surface area. Importantly, after 6 rounds of regeneration, the adsorbance of MB onto $Ni_{0.9}Mn_{0.1}Fe_2O_4$ MNPs still maintained about 90% of the first adsorption capacity, indicating that $Ni_{0.9}Mn_{0.1}Fe_2O_4$ MNPs had excellent recycling performance.

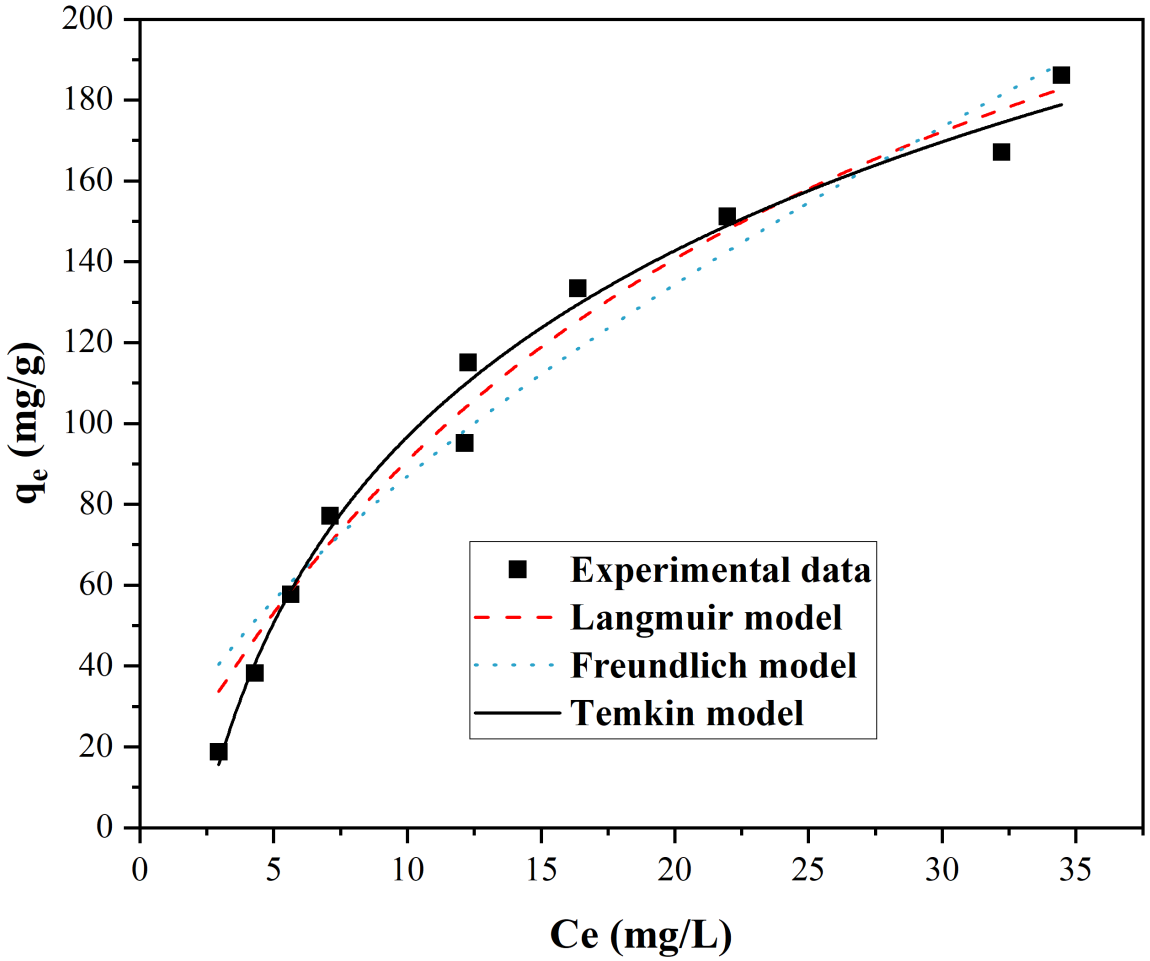

Fig 7. Adsorption isotherm of MB onto $Ni_{0.9}Mn_{0.1}Fe_2O_4$ MNPs at ambient temperature.

https://doi.org/10.1371/journal.pone.0321741.g007

Table 2. Simulative parameters of adsorption isotherms for MB onto $Ni_{0.9}Mn_{0.1}Fe_2O_4$ MNPs at room temperature.

adsorption isotherm model	R^2	fitting result	parameter	parameter value
Langmuir	0.9746	0.9714	q_{max}	312.0523
			K_L	0.0400
Freundlich	0.9484	0.9419	K_F	20.4684
			1/*n*	0.6281
Temkin	0.9865	0.9848	B_T	66.4165
			A_T	0.4287

https://doi.org/10.1371/journal.pone.0321741.t002

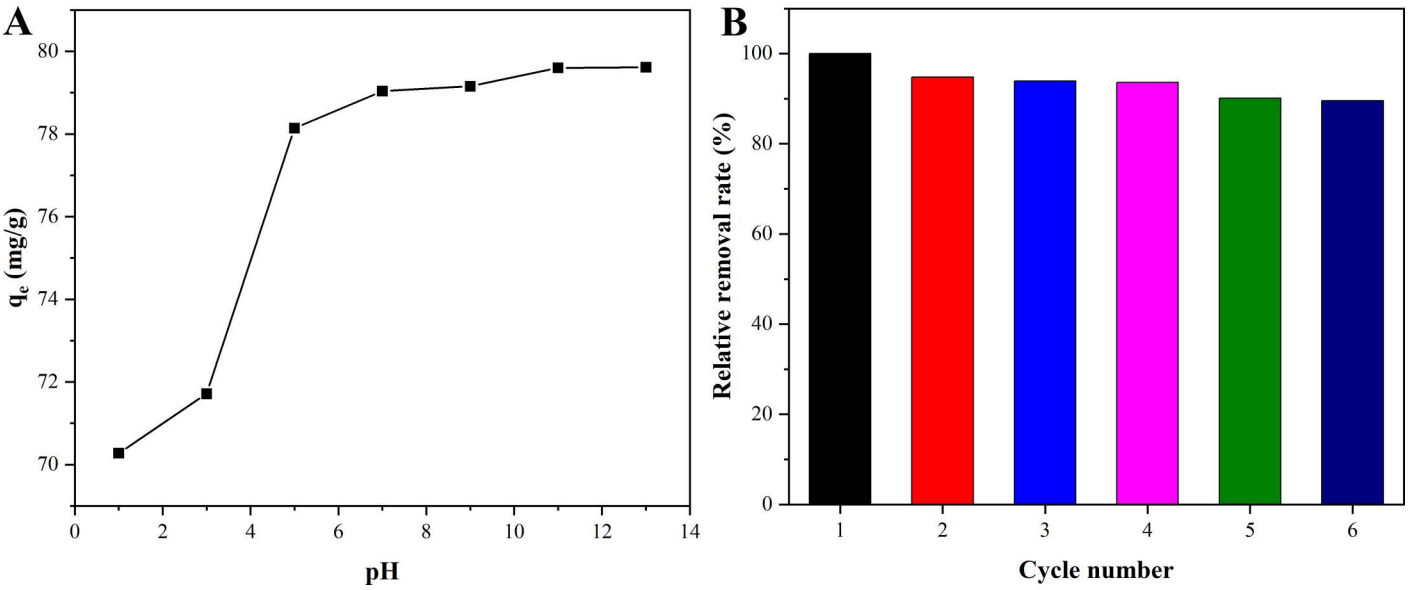

Fig 8. Influence of pH on the adsorbance of MB onto $Ni_{0.9}Mn_{0.1}Fe_2O_4$ MNP at room temperature (A) and the regeneration of $Ni_{0.9}Mn_{0.1}Fe_2O_4$ MNPs (B).

https://doi.org/10.1371/journal.pone.0321741.g008

Table 3. Comparison of the congeneric adsorbents for MB adsorptions.

Adsorbent	Adsorption capacity (mg/g)	Reference
$Co_{0.5}Zn_{0.5}Fe_2O_4$ MNPs	189.1	[41]
$MnFe_2O_4$ MNRs	102.3	[42]
$Co_{0.8}Cu_{0.2}Fe_2O_4$ MNPs	174.2	[43]
$Co_{0.4}Cu_{0.2}Zn_{0.4}Fe_2O_4$ MNPs	140.4	[44]
$Mg_{0.5}Cu_{0.5}Fe_2O_4$ MNPs	123.8	[45]
$Ni_{0.9}Mn_{0.1}Fe_2O_4$ MNPs	312.1	This work

https://doi.org/10.1371/journal.pone.0321741.t003

The congeneric adsorbents related for MB adsorptions were summarized and were listed in Table 3. Compared with the congeneric adsorbents, including $Co_{0.5}Zn_{0.5}Fe_2O_4$ MNPs, $MnFe_2O_4$ MNRs, $Co_{0.8}Cu_{0.2}Fe_2O_4$ MNPs, $Co_{0.4}Cu_{0.2}Zn_{0.4}Fe_2O_4$ MNPs, $Mg_{0.5}Cu_{0.5}Fe_2O_4$ MNPs, the adsorption capacity of MB onto $Ni_{0.9}Mn_{0.1}Fe_2O_4$ MNPs was almost 1.65 3.05 times of ones for the congeneric adsorbents, suggesting the promising application of $Ni_{0.9}Mn_{0.1}Fe_2O_4$ MNPs for the removal of MB.

3.3.4. ***FTIR spectrum.*** FTIR spectroscopy was used to indicate the reproductive property of $Ni_{0.9}Mn_{0.1}Fe_2O_4$ MNPs. The infrared spectra of MB (Fig 9A), $Ni_{0.9}Mn_{0.1}Fe_2O_4$ MNPs (Fig 9B), $Ni_{0.9}Mn_{0.1}Fe_2O_4$ MNPs after adsorption of MB (Fig 9C), and $Ni_{0.9}Mn_{0.1}Fe_2O_4$ MNPs recalcined at 400 °C for 2 h after adsorption (Fig 9D) were analyzed. As shown in the figure, there are five obvious characteristic peaks of 1032 cm^{-1},1122 cm^{-1},1170 cm^{-1},1340 cm^{-1}, and 1575 cm^{-1} on the infrared spectrum of MB. Compared with $Ni_{0.9}Mn_{0.1}Fe_2O_4$ MNPs unadsorbed MB, the infrared spectrum of the adsorbed $Ni_{0.9}Mn_{0.1}Fe_2O_4$ MNPs showed five characteristic peaks corresponding to MB in addition to the Fe-O characteristic peak at 590 cm^{-1}, which verified that MB was successfully adsorbed onto $Ni_{0.9}Mn_{0.1}Fe_2O_4$ MNPs. When $Ni_{0.9}Mn_{0.1}Fe_2O_4$ MNPs adsorbed MB were calcined at 400 °C for 2 h, the characteristic peak of MB in the infrared spectrum basically disappeared and meanwhile the characteristic peak of $Ni_{0.9}Mn_{0.1}Fe_2O_4$ MNPs reappeared, demonstrating that the regeneration of $Ni_{0.9}Mn_{0.1}Fe_2O_4$ MNPs could be realized after calcination.

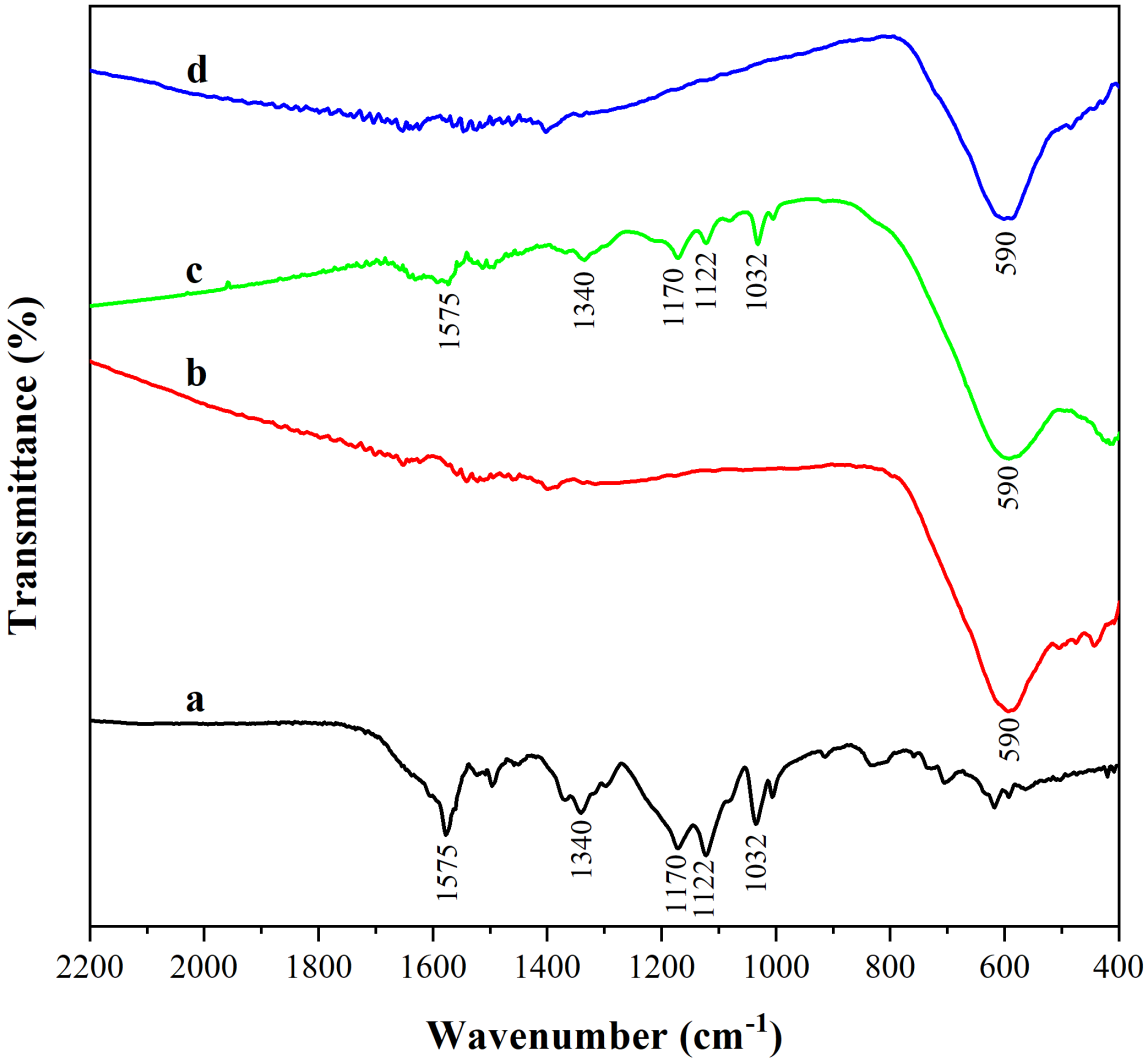

Fig 9. FTIR spectrum of MB (A), $Ni_{0.9}Mn_{0.1}Fe_2O_4$ MNPs (B), $Ni_{0.9}Mn_{0.1}Fe_2O_4$-MB (C) and $Ni_{0.9}Mn_{0.1}Fe_2O_4$ MNPs recalcined at 400 °C for 2 h after adsorption (D).

https://doi.org/10.1371/journal.pone.0321741.g009

4. Conclusions

(1) $Ni_xMn_{(1-x)}Fe_2O_4$ MNPs were prepared through the ethanol solution combustion-calcination process, and the as-prepared $Ni_{0.9}Mn_{0.1}Fe_2O_4$ MNPs under optimum preparation conditions (Fe^{3+} concentrations of approximately 0.85 M, the calcination temperature of 400 °C, calcination time of 2 h) with average diameter of about 35 nm, Ms of 21.66 emu/g, and the specific surface area of 136.5 m^2/g were selected for the removal of MB.

(2) Pseudo-second-order kinetic and Temkin models were the best fittings for the adsorption data of MB onto $Ni_{0.9}Mn_{0.1}Fe_2O_4$ MNPs at ambient temperature, indicating that the multi-molecular layer chemisorption process involving electron sharing or electron transfer was more likely to be the principal underlying mechanism for the removal of MB.

(3) The influence of pH on the adsorbance showed that the adsorption of MB on $Ni_{0.9}Mn_{0.1}Fe_2O_4$ MNPs could maintain a large adsorption capacity for MB in a range of pH > 5. The FTIR spectroscopy and regeneration performance proved

that $Ni_{0.9}Mn_{0.1}Fe_2O_4$ MNPs could be regenerated by calcination, and still maintain a high adsorption capacity even regenerated for 6 times, exhibiting the excellent reusability and stability of $Ni_{0.9}Mn_{0.1}Fe_2O_4$ MNPs.

Supporting information

S1 Fig. SEM morphology of $Ni_{0.9}Mn_{0.1}Fe_2O_4$ MNPs calcined at 400 °C with 20 mL ethanol and Fe^{3+} concentrations of 0.85 M.
(TIF)

S2 Fig. TEM image of $Ni_{0.9}Mn_{0.1}Fe_2O_4$ MNPs calcined at 400 °C with 20 mL ethanol and Fe^{3+} concentrations of 0.85 M.
(BMP)

Author contributions

Conceptualization: Zhou Wang, Zhixiang Lv.

Data curation: Zhongjun Pan.

Formal analysis: Zhongjun Pan, Zhou Wang.

Investigation: Zhongjun Pan.

Methodology: Zhou Wang, Zhixiang Lv.

Project administration: Zhixiang Lv.

Resources: Zhixiang Lv.

Supervision: Zhixiang Lv.

Validation: Zhongjun Pan, Zhou Wang.

Visualization: Zhongjun Pan, Zhixiang Lv.

Writing – original draft: Zhongjun Pan.

Writing – review & editing: Zhixiang Lv.

References

1. Urucu OA, Garosi B, Musah RA. Efficient Phytoremediation of Methyl Red and Methylene Blue Dyes from Aqueous Solutions by Juncus effusus. ACS Omega. 2025;10:1943–53. https://doi.org/10.1021/acsomega.4c07468
2. Wu J, Yao J, Zhu X, Zuo D, Zhang H, Jiang S, et al. Synthesis and characterization of zwitterionic hydrogels with Ag@g-C3N4 for adsorption-photocatalytic removal of methylene blue and methyl orange dyes. Adsorption. 2025;31:14. https://doi.org/10.1007/s10450-024-00560-w
3. Li X, Cao X, Wang H, Sun Y, Zhang S, Khodseewong S, et al. The promotion of the atrazine degradation mechanism by humic acid in a soil microbial electrochemical system. J Environ Manage. 2024;357:120767. https://doi.org/10.1016/j.jenvman.2024.120767 PMID: 38560953
4. Tian D, Cheng J, Pei X, Liu Z, Liu Q, Chen Q. Progress of organic wastewater degradation by atmospheric pressure gliding arc plasma technology: A review. AIP Adv. 2024;14:030702. https://doi.org/10.1063/5.0191470
5. Botle A, Salgaonkar S, Tiwari R, Ambadekar S, Barabde GR. Brief status of contamination in surface water of rivers of India by heavy metals: a review with pollution indices and health risk assessment. Environ Geochem Health. 2023;45:2779–801. https://doi.org/10.1007/s10653-022-01463-x PMID: 36583797
6. Abduljaleel Y, Amiri M, Amen EM, Salem A, Ali ZF, Awd A, et al. Enhancing groundwater vulnerability assessment for improved environmental management: addressing a critical environmental concern. Environ Sci Pollut R. 2024;31:19185–205. https://doi.org/10.1007/s11356-024-32305-1
7. Tripti T, Singh P, Rani N, Kumar S, Kumar K, Kumar P. Carbon dots as potential candidate for photocatalytic treatment of dye wastewater. Environ Sci Pollut R. 2024;31:6738–65. https://doi.org/10.1007/s11356-023-31437-0
8. Rai A, Sirotiya V, Mourya M, Khan MJ, Ahirwar A, Sharma AK, et al. Sustainable treatment of dye wastewater by recycling microalgal and diatom biogenic materials: Biorefinery perspectives. Chemosphere. 2022;305:135371. https://doi.org/10.1016/j.chemosphere.2022.135371 PMID: 35724717

9. Lin JY, Ye WY, Xie M, Seo DH, Luo JQ, Wan YH, et al. Environmental impacts and remediation of dye-containing wastewater. Nat Rev Earth Env. 2023;4:785–803. https://doi.org/10.1038/s43017-023-00489-8
10. Huang PN, Qi XJ, Duan XX, Jiang WQ, Yang NN, Zhi G, et al. Efficient arsenate capture using mixed-metal La/Zr-MOF internal complexation. New J Chem. 2024;48:5311–25. https://doi.org/10.1039/D3NJ05509D
11. Tanyol M, Yildirim NC, Alparslan D. Electrocoagulation induced treatment of indigo carmine textile dye in an aqueous medium: the effect of process variables on efficiency evaluated using biochemical response of Gammarus pulex. Environ Sci Pollut R. 2021;28:55315–29. https://doi.org/10.1007/s11356-021-14819-0
12. Zhai L-F, Hu Y, Xu S-Y, Guo H-Y, Sun M, Yu J, et al. Kinetics and mechanism study of dyes degradation in electric field-promoting catalytic wet air oxidation process. J Environ Manage. 2023;338:117843. https://doi.org/10.1016/j.jenvman.2023.117843 PMID: 37004485
13. Jadhav SP, Ayare SD, Gogate PR. Intensified degradation of tartrazine dye present in effluent using ultrasound combined with ultraviolet irradiation and oxidants. Environ Monit Assess. 2024;196:1–17. https://doi.org/10.1007/s10661-024-12561-x PMID: 38580863
14. Cong J, Xie X, Liu Y, Qin Y, Fan J, Fang Y, et al. Biochemical characterization of a novel azo reductase named BVU5 from the bacterial flora DDMZ1: application for decolorization of azo dyes. RSC Adv. 2022;12:1968. https://doi.org/10.1039/d1ra08090c PMID: 35425265
15. Zhou S, Jia Y, Fang H, Jin C, Mo Y, Xiao Z, et al. A new understanding on the prerequisite of antibiotic biodegradation in wastewater treatment: Adhesive behavior between antibiotic-degrading bacteria and ciprofloxacin. Water Res. 2024;252:121226. https://doi.org/10.1016/j.watres.2024.121226 PMID: 38309071
16. Chakrabarty S, Tamim A, Yılmaz M, Dhar PK, Mim RM, Dutta SK. Adsorption of Pb (II) ions from Aqueous Solution Using CuO-ZnO Nanocomposites. Chem Afr. 2023;6:1449–62. https://doi.org/10.1007/s42250-022-00554-7
17. Goswami MK, Srivastava A, Dohare RK, Tiwari AK, Srivastav A. Recent advances in conducting polymer-based magnetic nanosorbents for dyes and heavy metal removal: fabrication, applications, and perspective. Environ Sci Pollut R. 2023;30:73031–60. https://doi.org/10.1007/s11356-023-27458-4 PMID: 37195615
18. Aryee AA, Dovi E, Han RP, Li ZH, Qu LB. One novel composite based on functionalized magnetic peanut husk as adsorbent for efficient sequestration of phosphate and Congo red from solution: Characterization, equilibrium, kinetic and mechanism studies. J Colloid Interface Sci. 2021;598:69–82. https://doi.org/10.1016/j.jcis.2021.03.157 PMID: 33892443
19. Marey A, Gado WS, Soliman AG, Masoud AM, El-Zahhar AA, Al-Hazmi GAAM, et al. Efficient removal of methylene blue dye from wastewater specimen using polystyrene coated nanoparticles of silica. Inorg Chem Commun. 2024;160:112018. https://doi.org/10.1016/j.inoche.2024.112018
20. Chen X, Chai J, Yang X, Chai F, Tian MM. Amino acid-immobilized copper ion-modified carbon-based adsorbent for selective adsorption of bovine hemoglobin. J Chromatogr A. 2022;1680:463440. https://doi.org/10.1016/j.chroma.2022.463440 PMID: 36037577
21. Li HH, Sheng W, Haruna SA, Hassan MM, Chen QS. Recent advances in rare earth ion-doped upconversion nanomaterials: From design to their applications in food safety analysis. Compr Rev Food Sci F. 2023;22: 3732–64. https://doi.org/10.1111/1541-4337.13218
22. Ramu S, Kainthla I, Chandrappa L, Shivanna JM, Kumaran B, Balakrishna RG. Recent advances in metal organic frameworks-based magnetic nanomaterials for waste water treatment. Environ Sci Pollut R. 2024;31:167–90. https://doi.org/10.1007/s11356-023-31162-8 PMID: 38044404
23. Bhattarai MK, Ashie MD, Dugu S, Subedi K, Bastakoti BP, Morell G, et al. Block Copolymer-Assisted Synthesis of Iron Oxide Nanoparticles for Effective Removal of Congo Red. Molecules. 2023;28:1914. https://doi.org/10.3390/molecules28041914 PMID: 36838902
24. Pang L, Pi X, Zhao Q, Man C, Yang X, Jiang Y. Optical nanosensors based on noble metal nanoclusters for detecting food contaminants: A review. Compr Rev Food Sci F. 2024;23:e13295. https://doi.org/10.1111/1541-4337.13295 PMID: 38284598
25. Wu L, Wen W, Wang X, Huang D, Cao J, Qi X, et al. Ultrasmall iron oxide nanoparticles cause significant toxicity by specifically inducing acute oxidative stress to multiple organs. Part Fibre Toxicol. 2022;19:24. https://doi.org/10.1186/s12989-022-00465-y PMID: 35351185
26. Parastar Gharehlar M, Sheshmani S, Nikmaram FR, Doroudi Z. Synergistic potential in spinel ferrite MFe_2O_4 (M = Co, Ni) nanoparticles-mediated graphene oxide: Structural aspects, photocatalytic, and kinetic studies. Sci Rep. 2024;14:4625. https://doi.org/10.1038/s41598-024-55452-4
27. Chejara U, Prajapati A, Kumar A. Dielectric studies for rare earth doped magnesium ferrite material. Environ Sci Pollut R. 2023;30:98601–8. https://doi.org/10.1007/s11356-022-21688-8 PMID: 35799011
28. Long XY, Zhang ZJ, Li JY, Sheng D, Lian HZ. Controllable Preparation of $CuFeMnO_4$ Nanospheres as a Novel Multifunctional Affinity Probe for Efficient Adsorption and Selective Enrichment of Low-Abundance Peptides and Phosphopeptides. Anal Chem. 2017;89:10446–10453. https://doi.org/10.1021/acs.analchem.7b02476
29. Cheng P, Wang X, Markus J, Abdul Wahab M, Chowdhury S, Xin R, et al. Carbon nanotube-decorated hierarchical porous nickel/carbon hybrid derived from nickel-based metal-organic framework for enhanced methyl blue adsorption. J Colloid Interface Sci. 2023;638:220–30. https://doi.org/10.1016/j.jcis.2023.01.075 PMID: 36738545
30. Bukhari A, Ijaz I, Nazir A, Hussain S, Zain H, Gilani E, et al. Functionalization of Shorea faguetiana biochar using Fe2O3 nanoparticles and MXene for rapid removal of methyl blue and lead from both single and binary systems. RSC Adv. 2024;14:3732. https://doi.org/10.1039/d3ra07250a PMID: 38288151
31. Li Y, Pan S, Yu QM, Ding X, Liu RJ. Adsorption mechanism and electrochemical performance of methyl blue onto magnetic Ni(1-x-y)CoyZnxFe2O4 nanoparticles prepared via the rapid-combustion process. Ceram Int. 2020;46:3614–22. https://doi.org/10.1016/j.ceramint.2019.10.080
32. Akbari M, Jafari H, Rostami M, Mahdavinia GR, Sobhani Nasab A, Tsurkan D, et al. Adsorption of Cationic Dyes on a Magnetic 3D Spongin Scaffold with Nano-Sized Fe3O4 Cores. Mar Drugs. 2021;19:512. https://doi.org/10.3390/md19090512 PMID: 34564174

33. Ni Y, Deng P, Yin RT, Zhu ZY, Ling C, Ma MY, et al. Effect and mechanism of paclitaxel loaded on magnetic Fe_3O_4@mSiO_2-NH_2-FA nanocomposites to MCF-7 cells. Drug Deliv. 2023;30:64–82. https://doi.org/10.1080/10717544.2022.2154411
34. Liu T, Zhang ST, Wang Z, Xu YY. Preparation and characterization of α-Fe_2O_3/Fe_3O_4 heteroplasmon nanoparticles via the hydrolysis-combustion-calcination process of iron nitrate. Mater Res Express. 2022;9:045011. https://doi.org/10.1088/2053-1591/ac68c6
35. Lv AW, Lv X, Xu XY, Shao ZB. Tailored ultra-tough, antimicrobial and recyclable hydrogels based on chitosan and ionic liquid modified montmorillonite with different chain lengths for efficient adsorption of organic dyes in wastewater. Int J Biol Macromol. 2024;257:128752. https://doi.org/10.1016/j.ijbiomac.2023.128752
36. Zhao Y, Song Y, Li R, Lu F, Yang Y, Huang Q, et al. Enhanced Reactive Brilliant Blue Removal Using Chitosan-Biochar Hydrogel Beads. Molecules. 2023;28:6137. https://doi.org/10.3390/molecules28166137 PMID: 37630389
37. Dragan ES, Apopei Loghin DF, Cocarta AI. Efficient Sorption of Cu^{2+} by Composite Chelating Sorbents Based on Potato Starch-graft-Polyamidoxime Embedded in Chitosan Beads. ACS Appl Mater Interfaces. 2014;6:16577–92. https://doi.org/10.1021/am504480q
38. Agaguena A, Benbellat N, Khaoua O, Bendaikha T. Kinetic adsorption of methyl blue dye from aqueous solution by PVC/PVC-based copolymer containing quaternary amine. Anal Sci. 2023;39:1371–83. https://doi.org/10.1007/s44211-023-00356-y PMID: 37208560
39. Ling C, Wang Z, Ni Y, Zhu Z, Cheng Z, Liu R. Superior adsorption of methyl blue on magnetic Ni–Mg–Co ferrites: Adsorption electrochemical properties and adsorption characteristics. Environ Prog Sustain. 2022;41:e13923. https://doi.org/10.1002/ep.13923
40. Lugito G, Samadhi TW, Prakoso T, Lauda M, Tanujaya VL. Techno-economic and Environmental Analyses on Reduced Graphene Oxide modified Kapok Fiber as Oil. IOP Conf Ser: Mater Sci Eng. 2021;1143:012008. https://doi.org/10.1088/1757-899X/1143/1/012008
41. Deng P, Liu M, Lv Z. Adsorption mechanism of methyl blue onto magnetic Co0.5Zn0.5Fe2O4 nanoparticles synthesized via the nitrate-alcohol solution combustion process. AIP Advances. 2020;10:095005. https://doi.org/10.1063/5.0011573
42. Lv Z, Wang Z. A facile combustion process for the preparation of magnetic MnFe2O4 nanorods and their adsorption mechanism of methyl blue. AIP Advances. 2020;10:055106. https://doi.org/10.1063/5.0003108
43. Yin R, Zhang S, Xu Y, Xue J, Bi J, Liu R. Adsorption mechanism and electrochemical properties of methyl blue onto magnetic CoxCu(1–x)Fe2O4 nanoparticles prepared via an alcohol solution of nitrate combustion and calcination process. J Inorg Organomet P. 2021;31:3584–94. https://doi.org/10.1007/s10904-021-01986-3
44. Ouyang HZ, Pan SY, Liu AH, Wang Y, Zang ZZ, Liu YC, Liu DD. Preparation of magnetic cobalt-cuprum-zinc ferrites and their adsorption mechanism of methyl blue. Mater Res Express. 2022;9:025006. https://doi.org/10.1088/2053-1591/ac5079
45. He N, Lv Z, Wang Z, Zhang H, Wu S, Li Y, et al. Adsorption performances and electrochemical characteristic of methyl blue onto magnetic MgxCu(1-x)Fe2O4 nanoparticles prepared via the rapid combustion process. Water Air Soil Poll. 2024;235:310. https://doi.org/10.1007/s11270-024-07119-z